The DOI for this manuscript is doi: 10.1175/MWR-D-13-00259.1

Summer precipitation events over the western slope of the subtropical Andes

Maximiliano Viale[*] and René Garreaud

Departamento de Geofísica, Facultad de Ciencias Físicas y Matemáticas,

Universidad de Chile, Santiago, Chile.

Submitted to MWR
Revised October 2013

[*] Corresponding author address: Maximiliano Viale

Departamento de Geofísica, Universidad de Chile, Blanco Encalada 2002, Santiago, Chile.

E-mail: maxi@dgf.uchile.cl

Abstract

Summertime (DJF) precipitation over the western slopes of the subtropical Andes (32°-36°S) accounts for less than 10% of the annual accumulation but it mostly occurs as rain and may triggers landslides leading to serious damages. Based on 13-year of reanalysis, in-situ observations, and satellite imagery, a synoptic climatology and physical diagnosis reveal two main weather types lead to distinct precipitation systems.

The most frequent type (~80% of the cases) occurs when a short-wave mid-level trough with weak winds and thermally-driven mountain winds favor the development of convective precipitation during the daytime. The trough progresses north-west of a long-lasting warm ridge, which produces low-level easterly airflow that enhances its buoyancy as moves over the arid land of western Argentina toward the Andes. The weak winds aloft facilitate the penetration of the moist easterly flow into the Andes. Mid-level flow coming from the west side of the Andes is decoupled from the low-level maritime air by a temperature inversion, and thus provides little moisture to support precipitation.

The less frequent type (~20% of the cases) occurs when a deep mid-level trough and strong westerly flow produces stratiform precipitation. This type has a baroclinic nature akin of winter storms, except that they are rare in summer and there is no evidence of a frontal passage at low levels. The lifting and cooling ahead of the trough erode the typical temperature inversion over the Pacific

coast, and thus allows upslope transport of low-level marine air by the strong westerlies forming a precipitating cloud cap on the western slope of the Andes.

1. Introduction

Summer precipitation events over major mountain ranges are often of convective nature. They are controlled by synoptic-scale flow and thermally-driven mountain-scale circulations. For instance, the moisture source of convective storms over the central Andes (17°-23°S) is located over the lowlands to the east and is transported to the high terrain by the daytime plain-to-mountain breeze, which intensity and extent are modulated by the synoptic-scale zonal flow aloft (e.g. Garreaud 1999). Thermally-driven mountain circulations (e.g., Whiteman 2000) have also been suggested as a key factor controlling the small-scale spatial (<150km) and temporal variation of cloudiness and precipitation within the tropical central Andes (Giovannettone and Barros 2009), the Sierra Madres in Mexico (Giovannettone and Barros 2008) and the Himalayas (Barros et al. 2004). Passage of eastward-moving, extratropical disturbances during summertime can also produce precipitation over the mountains but their frequency is greatly reduced in subtropical latitudes (Garreaud and Ruttland 1997). In these cases, precipitation tends to be more stable and stratiform in nature.

The Andes cordillera is a tall mountain range extending along the west coast of South America from 10°N to 53°S and exerting a strong influence on the regional climate (e.g., Garreaud 2009). In this work we focus on precipitation occurring during austral summer months (December to February; DJF) over the western slope of the subtropical Andes (32°-36°S). In this range of latitudes the Andes is only ~200 km wide but its mean height exceeds 4000 m ASL (see Fig. 1b and 3c) thus acting as a climatic wall between central Chile to the west and the Argentina's lowland to the east (e.g., Prohaska 1976; Miller 1976; see also Fig. 1). Austral summer is the dry season in central Chile, so we anticipate that summer precipitation over the western slope subtropical Andes accounts for less than 10% of the annual total. Consequently, summer storms there have received less attention than their winter counterparts (Falvey and Garreaud 2007; Barrett et al. 2009; Viale and Nuñez 2011; Garreaud 2013; Viale et al. 2013).

During summer events, however, liquid precipitation can occur as high as 4000 m ASL over the mountains, quite further above than the typical snow line in winter (~2300 m ASL; Garreaud 2013). As a consequence, summertime, convective storms[1] have the potential to trigger debris flows or landslides on the steep slopes of the Andes, producing serious damages on mountain mining sites (e.g., Golder Associates 2009), international highways, and other facilities at the Andean foothills (e.g., Sepulveda and Padilla 2008). There is also evidence of

[1] Some of these events go unrecorded (or under-sampled) given their isolated, convective nature and the sparse station network at high elevation. For instance, light precipitation (less than 10 mm/day) was recorded in only two mountain stations in central Chile during a couple of events occurred when writing this manuscript (January 21 and February 8, 2013). These events, however, produced a sudden increase in the flow and sedimentary load of several Andean rivers causing a 2-day shutdown of the drinking water supply for the Santiago metropolitan area.

stratiform rain events during summer -more akin to winter storms- associated with strong mid-level westerlies affecting climbers of the many high peaks in this Andean region; these events have resulted in fatalities in the worst cases (C. Bravo 2013, personal communication).

The basic climatology and synoptic environment during summer precipitation events over the western slope of the subtropical Andes was addressed by Garreaud and Rutllant (1997). On the basis of low-resolution weather maps during 94 events recorded in a single mountain site between 1970 and 1992, they found two significant weather types differing in the intensity of the mid-level flow atop of the Andes: a through with strong westerlies and a weak trough with weak westerly or easterly winds. In the present work we aim at understanding the physical processes leading to summer precipitation events on the western slope of the subtropical Andes, an aspect not addressed by Garreaud and Rutllant (1997). To this end, we reexamine the attending synoptic conditions using state-of-the-art reanalysis data and radiosonde observations during 13 summers between 1998 and 2010, describe the cloudiness pattern and local conditions using high-resolution satellite imagery and an expanded surface observation network, and perform a trajectory analysis to determine the water vapor source of these storms.

The paper is organized as follows. In section 2 we present the observational data and explain the cluster analysis used to identify the main weather types associated with precipitation over the west side of the subtropical Andes. Section

3 provides a climatological overview of precipitation and cloudiness over the subtropical Andes. In section 4 we describe the synoptic and regional conditions associated with summer precipitation events while in section 5 we address the moisture sources and the physical mechanisms responsible for summer precipitation. The results are summarized in section 6.

2. Data and Methods

a. Surface and radiosonde data

Figure 2a shows the location of 153 surface stations with daily precipitation records (at 1200 UTC / 09:00 LT) used in this study, superimposed on a topographic map of the subtropical Andes (32°-37°S) and the adjacent lowlands. Most of these stations are located at low elevations in central Chile (114 stations; see details on Table 1) and western Argentina (32 stations, Table 1). Only seven stations are located on the Andes Mountain, with elevations higher than 1300 m ASL and less than 50 km from the Andean crest, which we refer hereafter as mountain stations. A common period from 2005 to 2010 was used to construct long-term mean fields, but the whole period 1998-2010 was used for the synoptic climatology analysis.

To explore the diurnal variation of wind and moisture in the mountain, we used data from Lagunitas (LAG) station on the western slopes and from Punta de Vacas (PVA) station on the eastern slopes of the Andes (see Table 1). The availability of data at LAG and PVA is for the 1998-2010 period. LAG records observations every 3 hours, while PVA has only three observations per day (09, 12 and 00 UTC).

There are four radiosonde stations surrounding the subtropical Andes (shown in Fig. 1, details in Table 2): two close to the foot of the Andes at 33°S (Santo Domingo (Chile) and Mendoza (Argentina) and two farther to the east on the Argentinean plains (Santa Rosa and Cordoba). Their data and metadata were obtained from the Integrated Global Radiosonde Archive (IGRA), a global upper-air dataset from the National Climatic Data Center (NCDC) (Durre et al. 2006). For the composite analysis of vertical profiles, radiosonde data from the 1200 UTC launches were homogenized in eleven standard vertical levels (from 1000 hPa to 200 hPa by performing lineal vertical interpolation using data from available levels) for wind, height, and temperature variables, and in five standard levels (from 1000 hPa to 500 hPa) for the humidity variable.

b. Gridded and satellite data

For the synoptic analysis, we used two global gridded datasets from the National Centers for Environmental Prediction: (1) the Climate Forecast System (CFSR) Reanalysis data and (2) the Global Data Assimilation System (GDAS). The CFSR data belongs to the last generation of available global reanalysis, with a high-resolution grid generated by a coupled atmosphere-ocean-land surface-sea ice system (Saha et al. 2010). Six-hourly average pressure-level fields are available on a 0.5°×0.5° lat-lon grid. Surface fields have a 0.32° grid spacing. CFSR was employed to construct the synoptic maps and vertical profiles of our synoptic climatology. The GDAS data are available on 1°×1° lat-lon grid every 6 h, and with 23 vertical level from 1000 hPa to 20 hPa. GDAS was employed for the trajectory analysis using the Hybrid Single-Particle Lagrangian Integrated Trajectory (HYSPLIT) model (Draxler and Rolph 2011).

To estimate the long-term mean, fine-scale orographic effect on cloudiness, we used data from the Moderate Resolution Imaging Spectroradiometer (MODIS) sensor on board of the Aqua and Terra satellites passing over the subtropical Andes twice daily. Specifically we employed the binary cloud-flag included in the fractional snow cover field of the Snow Cover Daily L3 Global Grid V5 product (MOD10A1 and MYD10A1), which informs on the presence of clouds on 500 m × 500 m grid by combining visible and infrared reflectance (Hall and Salomonson 2006, Hall et al. 2006). This binary cloud-flag is available twice daily since 2002 at about 1500 UTC (1200 LST) and 1900 UTC (1600 LST) for the Terra and Aqua satellites, respectively, at the National Snow and Ice Data Center (http://nsidc.org/). The version 5 reprocessing of this dataset used an improved MODIS cloud mask in order to mitigate the snow/cloud discrimination problem (Hall and Riggs 2007). This problem is minor during summer in the subtropical Andes, when the snow cover is limited to the higher mountains (i.e., higher than 5000 m). GOES-13 visible images (1 km resolution at nadir) were also used to illustrate individual cases, and CloudSat reflectivity data level 3 product, derived from 2B-GEOPROF reflectivity data, provides a climatological background of vertical structure of cloud during summer across the Andes (http://climserv.ipsl.polytechnique.fr/cfmip-obs/).

c. Cluster analysis

The synoptic-climatology developed in this work pretends to identify and describe the large-scale circulation and cloudiness patterns that characterize summertime precipitation events over the western side of the subtropical Andes. To this effect, we began by identifying rainy days as those when the sum of daily precipitation at Lagunitas (LAG) and El Yeso (YES), the two higher stations on the western slope of the Andes, was greater than 0.5 mm. This criterion resulted in 114 rainy days during austral summer months (DJF) from 1998 to 2010. Granted, 0.5 mm/day is a low value but, as we show later and suggested by Romatschke and Houze (2013), summer precipitation in this region mostly comes from small convective precipitating cloud systems, so a low accumulation could imply precipitation coming from a sector adjacent to the core of convective cloud or from an old system moving above the station.

Using this pool of 114 rainy days, we performed a cluster analysis of the 500 hPa geopotential height (Z500) in the domain 60°S-0° and 125°W-55°W. The cluster analysis employed the inverse spatial correlation as a pairwise distance and then the ward algorithm (minimum variance algorithm) for computing the distance between hierarchical agglomerated groups (e.g., Wilks, 1995). After applying this automatic method and according to the dendrogram plot of the hierarchical cluster tree, we found three major clusters (1, 2 and 3) with significant separation among them. Nevertheless, visual examination of the mean Z500 for each group, as well as other fields at lower levels, suggested that groups 2 and 3 represent essentially the same weather type, so we decided to merge them. Thus, we emphasize that the cluster analysis was used in support of our visual inspection of weather maps from where the two main modes of circulation associated with rainfall in our target area are readily evident. The main features of these two groups are described in section 4.

3. Climatological aspects

Before describing the synoptic and regional-scale features of the rainy days over the western subtropical Andes, in this section we provide an overview of the mean climate conditions during summer months (DJF) complementing previous work by Prohaska (1976), Miller (1976) and Garreaud and Ruttland (1997). Dry, relatively cool conditions and low-level maritime shadow clouds prevail to the west of the Andes (central Chile and the Pacific coast) in connection with the SE Pacific subtropical anticyclone (Fig. 1). In contrast, the mean low-level northerly flow over the interior of the continent leads to more humid and warm conditions, and vertically-developed clouds (convection) to the east of the Andes (western Argentina).

A marked zonal gradient in precipitation is evident in the summer (DJF) mean precipitation field constructed using station data (Fig. 2a). Between 32°-35°S, the coastal and lowland areas of Chile receive less than 15 mm/season, concentrated in a handful of days and representing less than 10% of the annual accumulation (Fig. 2b,c). Higher up over the subtropical Andes, mean summertime precipitation increases to ~40 mm in LAG and ~20 mm in YES on the western slopes, and to ~15 mm in PVA and POL immediately to the east of the crest (Fig. 2a), often occurring in only 5-10 days per season (Fig. 2b). The summer precipitation in these mountain stations still represents less than 10% of the annual total (Fig. 2c) but these storms bring rainfall (instead of snow) above 3500 m ASL (section 4b) having the potential for trigger localized debris flow given the steep slopes and the soil characteristics. Along the eastern foothills of the Andes the summer mean precipitation increases to over 100 mm (Fig. 2a), more evenly distributed in 30-40 days (Fig. 2b) and accounting for 50-60% of the annual accumulation (Fig. 2c).

The summertime fine-scale cloudiness pattern was obtained from the cloud frequency at 12 and 16 LST (Fig. 3) derived from the 500 m resolution MODIS cloud-flag product. Around noon (Fig. 3a,c), clouds are quite infrequent (<10%) over the subtropical Andes with the exception of a conspicuous band of high frequency (>40%) along the eastern first rise of the mountain range (the band roughly follows the 3000 m ASL contour in the Argentinean side). By late afternoon (Fig. 3b,c) the cloud frequency increases by 10-20% over the mountain range, reaching up to 40% over the highest terrain, consistent with the convergence of thermally-driven mountain winds flowing from both slopes. The strong control of topography on clouds can be noted in the afternoon plan-view map (Fig. 3b) and the afternoon cross-barrier section at one specific latitude (Fig. 3d), which suggest the development of thermally-driven mountain wind systems at different scales (e.g., Whiteman 2000). For example, the long and narrow maximum of cloud frequency over the eastern slopes suggests the development of a large-scale mountain-plain wind in this region; on the other side, local minimum over deep valleys and local maximum over highest peaks suggest the development of the small-scale upslope and up-valley wind systems.

Given its resolution, the CFSR only captures the large-scale diurnal mountain circulation over the subtropical Andes but not the fine-scale mountain circulations. Figure 4 shows the summer mean 10-m wind vectors at the extremes of the diurnal cycle, featuring upslope flow over both sides of the Andes converging just to the east of the ridge during the afternoon and the reversed pattern (downslope flow and divergence atop of the mountain) at dawn (Figs. 4a,b). This summer mean diurnal cycle of winds is supported by observations at the LAG site on the western slope (Fig. 4c). Such marked inflow to the Andes is highly recurrent and yet precipitation is very infrequent in this area as a result of the low moisture content and high static stability farther aloft. In other words, moisture and mid-level instability (favored by the presence of a through) are key ingredients for producing rainfall over the ridge and western slope of the subtropical Andes.

4. Synoptic circulation and local conditions during rainy days

a. Mean fields

As described in section 2c, the automatic cluster technique, complemented with individual inspection of each event, classified each summer-season rainy day over the western subtropical Andes into two main groups according to the attending synoptic-pattern. For reasons that are explained now, the groups are termed Trough-Weak Winds (TWW, the more frequent pattern) and Trough-Strong Westerlies (TSW). There is enough coherence within each group so that we can describe their main characteristic using the intra-group mean fields. The statistical significance of the mean composites was assessed by computing the standardized anomalies (departure from climatology divided by standard deviation) at each grid box.

Figure 5 shows the mean 500 hPa geopotential height (Z500) and temperature (T500) for each group. The TWW condition prevailed on 93 rainy days (82% of the total), most often grouped in 2-4 consecutive rainy days. At 500 hPa, TWW cases feature a short-wave trough just to the west of the subtropical Andes and a long-wave ridge farther to the south (Fig. 5a). Consistently, the Z500 and T500 anomaly fields (Fig. 5b) exhibit a dipole between subtropical and extratropical South America ($\pm 0.6\sigma$). A closed, cold-core low was found at mid- and upper-levels in 78% of the individual TWW cases, so this pattern often corresponds to a cut-off low passing to the north of a warm ridge that tend to remain stationary for several days over southern South America.

The less-frequent TSW cases (18%) are associated with a deep, mid-level trough with its axis oriented from NW to SE crossing the Andes at subtropical latitudes (Fig. 5c). A mid-level, warm ridge is located upstream of the trough over the southeast Pacific. Standardized anomalies of Z500 exceeding -1σ extend over most of southern South America and are collocated with significant cold anomalies at 500 hPa (Fig. 5d), indicative of the baroclinic character of the TSW pattern. Only 21 of the 114 rainy days were classified as TSW and 12 of them are grouped in a sequence of 2 or 3 days, so we found only 14 events in 13 years (i.e., approximately 1 event per summer). These numbers assert that baroclinic waves causing precipitation over the western slope of the subtropical Andes are an unusual situation in summer. The opposite occurs in winter, when most of the precipitation events are associated with this synoptic pattern (e.g., Falvey and Garreaud 2007; Viale and Nuñez 2011).

The differences in the Z500 field between TWW and TSW cases lead to distinct mid-level circulation over the subtropical Andes that are evident in the polar plots of Fig. 6. There we present the observed zonal and meridional wind components at 500 hPa for each individual case at the four radiosonde stations surrounding the subtropical Andes. The 500-hPa winds in the TWW cases are weaker than average and have variable directions. At Santo Domingo, just to the west of the Andes, the wind speed in TWW cases generally does not surpass the 5 ms^{-1} and almost half of the cases exhibit an easterly component. In contrast, the 500-hPa wind during TSW cases is predominantly west-northwest at the four stations, with a mean magnitude of the order of 15 ms^{-1}, well above the summer mean in each station.

The 850-hPa composite means of selected fields reveal the low-level structure associated with the TWW and TSW cases (Fig. 7) (The moisture field is described later in section 5). The most salient features in the low-level composite for the TWW cases (Fig. 7a) are the warm, anticyclonic anomalies over southern South America under the mid-level ridge (quasi barotropic structure), and the weak negative temperature anomalies on the northern Argentina, suggesting a postfrontal situation. Farther to the northwest, there are negative geopotential anomalies over the subtropical Pacific coast. Nevertheless, the composite 850 hPa anomalies in this group are weak (standardized values less than 0.3) and eventually disappear at lower levels. The 850 hPa wind shows a clearly defined anticyclonic circulation over central Argentina (centered at 35°S, 60°W) producing strong flow directed from the Atlantic toward the eastern foothills of the subtropical Andes (Fig. 7b). This flow pattern often remains stationary for 3-7 days. Along the Chilean coast, southerly winds prevails but with a weak offshore component.

For TSW cases, large negative geopotential anomalies are found over central Argentina downstream of the subtropical Andes and to the west of the mid-level trough axis, while positive anomalies prevail over the southern Pacific (Fig. 7c). There are cold anomalies along the Pacific west coast, with maximum departures just to the west of the Andes, that project eastward into Argentina to the south of 40°S. To the northeast of the low-level trough over central Argentina there is a band of positive temperature anomalies extending from the eastern slope of the Andes towards the south Atlantic. The contrast between cold and warm anomalies over central Argentina signals the presence of a cold front, also evident in the convergence of low-level flow in Fig. 7d. The low-level cold front, however, cannot be identified over the Pacific sector. Likewise, geopotential height anomalies below 850 hPa are very small to the west of the Andes (and tends to disappear near the surface) but they remain significant to the east (not shown). Also note that to the east of the Andes, the synoptic pattern for the TSW rainy cases is similar to the early stage (one or two days before) of cold air incursions into tropical latitudes described by Garreaud and Wallace (1998) which, in turn, lead to summertime convection over La Plata basin where the prefrontal northerly low-level jet converge with the cold southerlies (e.g., Romatschke and Houze 2010).

b. Mean vertical profiles

Relevant details on the vertical stratification during the TWW and TSW rainy events can be inferred from the SkewT-logP graphs and vertical profiles in Figures 8 and 9, respectively. During TWW days, the depth and intensity of the low-level stable layer in Santo Domingo are not altered with respect to the climatological values (Figs. 8a and 9a). The Mendoza sounding reveals a slight warming in the lower levels relative to the days before and the summer mean (Fig. 9b), which is also present at the Santa Rosa and Cordoba soundings (not shown). At the Andes crest level (about 500 hPa) both Santo Domingo and Mendoza soundings feature weak winds (Fig. 8), a slight cooling (Fig. 9b) and reduced stability (Fig. 9a) relative to the previous days in connection with the approaching short wave trough. The mean freezing level during TWW cases is about 3900 m ASL, well above than the typical value during winter storms (about 2300 m ASL; Garreaud 2013).

During TSW events, the Santo Domingo mean sounding shows a marked reduction in the depth of the low-level stable layer that prevails in this region (Fig. 8a) and the temperature inversion was absent in most of these days (Fig. 9a). This is a consequence of the strong cooling above 850 hPa that occurs in the TSW-rainy days in connection with the passage of a deep trough (Figs. 8a and 9b). Yet, the mean freezing level during TSW cases is ~3300 m ASL. East of the Andes, the Mendoza mean sounding reveals a tropospheric-deep cooling of about 2.5°C/day (Figs. 8b and 9b). The wind profiles show the strong NW at mid-levels veering to W at higher levels, and southerly winds at lower levels in both stations.

c. Local conditions

In this subsection we describe the precipitation and cloudiness distributions during rainy days classified as TSW or TWW. To this effect, Table 3 presents basic statistics of the precipitation at the mountain stations. At our reference stations on the western slopes (LAG and YES) TWW cases are the most frequent and account for 80% and 44% of the summer precipitation respectively. Conversely, TSW cases are less frequent and account for 20% of the precipitation at LAG but 55% at YES. A nearby but lower station (Riecillos) has far less rainy days than Lagunitas (27 versus 122) but they show a similar distribution between

TSW and TWW cases. East of the crest line most of the summer rainfall over the Argentinean stations is associated with neither TSW nor TWW cases, and largely suppressed during TSW cases.

Rainy episodes in the Chilean mountain stations tend to be simultaneous under TSW conditions, suggesting spatially uniform precipitation over the western side of the subtropical Andes. Under TWW conditions, in contrast, there is a sizable number of days when rainfall is recorded at LAG exclusively, suggesting a convective nature of these events. The large number of rainy days and summer accumulation in this station also imply local-scale orographic effects that favor convection there, an aspect beyond the scope of this paper. Daily mean precipitation in Table 3 suggest that rain is more intense in TSW than in TWW cases. Nevertheless, this comparison could be misleading given the convective nature of rainfall in TWW cases.

Cloud frequency during TWW cases is higher on the eastern side of the Andes than over the western side, where they prevail over the highest terrain only (Fig. 10a,d). A marked diurnal cycle in clouds occurs in TWW cases with afternoon cloud frequency being above normal conditions (c.f., Figs. 10d and 10f). These features, along with the more variable/discontinuous precipitation records among mountain stations, further support the convective nature of precipitation during TWW cases. Figure 11a illustrates the convective, isolated character of the cloudiness limited to the Andes in a TWW day on the basis of GOES-13 visible imagery.

In contrast, cloud frequency during TSW cases is relatively uniform over the western side of the Andes (Figs. 10b,e) with values above 50% over terrain higher than ~2000 m ASL (including the high coastal mountains in the Chilean side) but also over deep Andean canyons. Over the western slope of the Andes, there is a minor morning-to-afternoon increase of cloudiness. Such cloud pattern, along with the more uniform/simultaneous rainfall at LAG/YES and the strong mid-level westerlies during TSW cases, suggests the formation of a nimbus-stratus cap over the western side of the Andes causing widespread precipitation over high terrain and dissipating downstream. Figure 11b illustrates this situation on the basis of GOES-13 visible imagery for one TSW case.

5. Moisture sources and physical mechanisms

In this section we explore the origin of the water vapor that precipitate in both TWW and TSW cases as well as the physical mechanisms leading to summertime precipitation over the western slope of the Andes.

a. TWW cases

The composite anomalies of the 700 hPa specific humidity for the TWW cases are shown in Fig. 7b, and exhibit a broad area of positive values over the subtropical Andes linked with moisture advection from northeast and moist-air damming east of the Andes. The mean moisture profile at Santo Domingo (Fig. 12a) indicates a uniform moistening at low and mid levels during TWW cases with respect to summer mean conditions. Farther east of the subtropical Andes there are weak negative anomalies collocated with the region of mean easterly flow over central Argentina (Fig. 7c). Such mid-level drying is confirmed by the Cordoba and Santa Rosa soundings (not shown), and consistent with the quasi-stationary postfrontal anticyclone and the disappearance of the northerly prefrontal low-level jet that brings moist air to this region (Vera et al. 2006). Closer to the eastern foothills, the Mendoza mean TWW sounding (Fig. 12b) shows near average moist conditions in the low-middle troposphere. Note in Fig.12 that actual mean value of specific humidity at 700 hPa to the east of the Andes is about 4 gr/Kg, twice as large as its counterpart to the west (i.e., the Santo Domingo sounding).

As shown in Fig. 13, the specific humidity (q_{sfc}) at LAG station on the western slope of the Andes is fairly higher in the TWW days than in non-rainy or TSW cases during the whole day, and it is also much higher than the specific humidity observed in the 850-700 hPa layer of the free atmosphere by the coastal sounding (Santo Domingo). Early in the morning, q_{sfc} at LAG is slightly lower than the specific humidity at PVA station (on the eastern slopes of the Andes and similar altitude, Fig. 13a) but in the afternoon, when the inflow toward the mountain becomes active[2], rather uniform moisture values are observed on both slopes during TWW days (Fig. 13b). By evening, q_{sfc} at LAG is slightly higher than its counterpart at PVA and much higher that the low-level moisture in Santo

[2] During non-rainy and TSW days specific humidity at LAG also tends to increase from morning to afternoon but it never reaches the values in TWW cases or those at PVA.

Domingo (Fig. 13c). Overall, this comparison of diurnal values of q_{sfc} on both slopes and on the Pacific coast suggests that continental sourced moisture is a major ingredient in TWW precipitation events over the western slope of the Andes.

The moisture source during TWW cases is further studied using a back-trajectory analysis employing HYSPLIT/GDAS (section 2b). Figure 14a shows the trajectories for the last 48-hr of air parcels arriving (arrival time: 21 LT) at 6 endpoints over the subtropical Andes at 4 km ASL (three points at each side) for each TWW rainy days in the period 2005-2010. For nearly all cases, air parcels arriving to the east side of the Andes come from Argentina between 1-2 km ASL and have a high moisture content (>6 gr/kg). As air moves over the warm and arid land it has a large diurnal variation in its temperature, rise around 1000 m during the afternoon, and exhibits a positive trend in the equivalent potential temperature (Fig. 14b-e). The increase in θ_e along the parcels' trajectories and the low-level warming over the western Argentina (Fig. 9b), strongly suggest a build-up of thermodynamic instability in this region during the 24-48 hr before the rainy episodes at LAG/YES.

Air parcels arriving to the western slope have a more diverse origin. While some trajectories originate over Argentina and cross the Andes, most of them come from the west and they previously resided over north-central Chile between 2 and 3 km ASL. Trajectories from the west exhibit a weaker diurnal variation in temperature and have low moisture content (< 4 gr/Kg), well below the values recorded at the mountain station (Fig. 13). Therefore, we suspect there is significant mixing and transport of continental, moist air crossing the mountains during TWW cases, but the low resolution of GDAS analysis data (in which the trajectories are based) cannot resolve these small-scale processes over such complex topography.

The continental moisture source for precipitation during TWW cases is supported by the daily composite zonal moisture flux (*uq*) profile, calculated from CFSR data at each side of the Andes (Fig. 15). The mean zonal moisture transport to the west of the Andes is very small in TWW cases (Fig. 15a), slightly negative (i.e., from the east) below 700 hPa and near 0 above that level. Over the eastern side, there is easterly low-level moisture transport (toward the Andes) regardless of the synoptic classification. Indeed, easterly moisture transport below 800 hPa is even stronger in TSW cases and non-rainy days than in TWW days (Fig. 15b). Nevertheless, the easterly transport in TWW cases encompasses a deep layer from the surface to ~650 hPa, favored by weak winds aloft.

b. TSW cases

The TSW mean anomalies of specific humidity at 700 hPa mean features positive anomalies just to the west of the subtropical Andes and negative anomalies to the east (Fig. 7d). This cross-mountain dipole in 700 hPa moisture anomalies is in good agreement with the vertical profiles of moisture anomalies derived from the Santo Domingo and Mendoza radiosondes (Fig. 12). The Santo Domingo profile further reveals that the maximum moisture anomalies upstream of the

Andes occurs around 700 hPa. Likewise, the maximum drying at Mendoza occurs at 700 hPa as a result of a Fohen effect (locally known as Zonda wind, Seluchi et al. 2003) instigated by the strong westerly winds crossing the subtropical Andes. Farther east over the Argentinean plains, low- and mid-level moisture recovers to near-average values (not shown).

The back-trajectory analysis for the TWW cases is shown in Fig. 14f-j. In all cases, air parcels reaching both west and east endpoints come from the west side of the Andes, often from the coast of central Chile. The time series of the parcel's mean vertical position reveal that air parcels generally reside around 1000 m ASL in the 36-42 hour period before a rapid ascent over the western slope of the Andes during the rainy afternoon.

This analysis, together with the vertical profile of moisture anomalies at Santo Domingo, suggests that the water vapor that precipitates over the western slope of the Andes during TSW cases originated in the marine boundary layer (MBL) along the Chilean coast, being transported upward by strong upslope flows ahead of the approaching trough and experienced a pseudo-adiabatic cooling (Figs. 14g-j) over the Andean west side. The moisture in the MBL is generally confined by a persistent inversion temperature at around 900 hPa (Rahn and Garreaud 2010) but, as noted in section 4b, the inversion is weak (if any) during TSW in connection with the passage of the deep mid-level trough over this region.

6. Conclusions

This study has examined the synoptic- and regional-scale conditions during summertime (DJF) precipitation events over the western slopes of the subtropical Andes as recorded by high-elevation stations in that region. Austral summer is the dry season in central Chile and the subtropical Andes, and it accounts for less than 10% of the annual accumulation concentrated on a few events of 1-3 days of duration. Nonetheless, summertime precipitation occurs under warm conditions producing rainfall up to 4000 m ASL (well above the freezing level during winter storms) and thus has the potential to trigger debris flow or landslides on the steep slopes of the Andes. There are also a few cases when summer precipitation is accompanied by (relatively) cold conditions and strong winds affecting climbers and other activities high in the Andes.

By examining high resolution reanalysis data and satellite imagery, as well as surface and upper-air observations at both sides of the subtropical Andes, we found two main weather patterns associated with precipitation events in the western side of the mountain, termed as Trough Weak Winds (TWW, ~80% of the cases) and Trough Strong Westerlies (TSW, ~20% of the cases). These patterns broadly coincide with those previously identified by Garreaud and Rutllant (1997). Here we deepened and expanded the description of these patterns and provided a dynamical interpretation of their nature, orographic control and moisture sources.

The main features of TWW and TSW cases are schematically synthesized in Fig.

16 by a zonal cross section at subtropical latitudes. Let us consider first the non-rainy conditions that prevail most of the summer days, dominated by moderate zonal flow at mid- and upper-levels over the subtropical Andes (Fig. 16a). To the west of the mountains, large-scale subsidence over the southeast Pacific produce stable, dry conditions over central Chile and a marked temperature inversion offshore. The moist air in contact with the ocean is vertically limited by this inversion and partially confined in the horizontal by a coastal range of about 1000 m ASL. Consistently, moist air transport from the west towards the Andes is small. To the east of the Andes much more humid and warm conditions prevail. Daytime upslope winds over the eastern slopes transport moist air but their progress toward the mountains is limited by the westerlies aloft and the high altitude of the barrier. The limitation of the moist advection from the Argentinean side is likely caused by a capping effect on the eastern foothills (trough forced subsidence or elevated mixed layers mechanisms) as has been observed in the lee of the Andes and other ranges (Carlson et al. 1983, Medina et al. 2010, Rassmussen and Houze 2011). Such pattern explains the low frequency (<20%) of clouds atop of the Andes during non-rainy afternoons and a well-defined band of high frequency (>60%) of clouds along the eastern slopes.

The most frequent TWW cases occur in association with an approaching shortwave trough and features easterly winds or very weak westerlies atop of the subtropical Andes (Fig. 16b). Although the trough in these cases is rather weak its cold core contributes to destabilize the tropospheric midlevel layer over the Andes. Farther south, a warm, long-wave ridge remains quasistationary over southern South America. The attending low-level anticyclone produces a deep layer (surface to 700 hPa) of easterly-northeasterly flow that enhances its buoyancy as it moves over the arid land of central-western Argentina toward the Andes. Since in these cases the mid-level flow atop of the Andes is very weak, the synoptic low-level easterly winds, that bring moist and increasingly less stable air from the continent, can penetrate well into the mountains reaching the crest line and the western slope of the Andes. Similar to the non-rainy days, the midlevel airflow coming from the western side of the Andes is decoupled from the near-surface maritime air (Fig. 16b,c), and may provide less moisture to convection than its eastern counterpart. The convection is released with a mixture of dry western- and moist eastern-sourced air within the unstable midlevel environment of the mid-level trough over the western slopes.

The less frequent TSW cases (about one event per summer) occur in association with a deep mid-level trough and strong westerlies atop of the subtropical Andes (Fig. 16c). These types of summer precipitation events have a baroclinic nature and bear resemblance to winter storms, except there is no evidence of a frontal passage at low levels over the east Pacific / central Chile. The approach of the mid-level trough and cold air aloft toward the Andes plays a crucial role in these events. First, it decreases the subtropical subsidence (or even produces ascent) weakening (or destroying) the low level temperature inversion. Secondly, moist, marine air can penetrate into central Chile being transported upward by the strong westerly flow impinging on the subtropical Andes. A stratiform cloud cap thus forms atop of the Andes eventually raining out over the high terrain of the western slopes. Consistently, precipitation in TSW cases tends to be widespread and light. Forced subsidence downstream of the crest line tends to dry the eastern slope of the Andes dissipating the cloud band along the Argentinean foothills and suppressing rainfall in that region.

The proposed conditions leading to TWW and TSW precipitation events were based mainly on the new CFSR reanalysis data, whose horizontal resolution would be not high enough to resolve small-scale orographic effects and so limit our conclusions. Further studies using high resolution model simulations for representative cases, and enhanced radiosonde observations on both slopes and foothills of the narrow subtropical Andes, are needed to refine and test these physical mechanisms proposed in this study.

Acknowledgments. We acknowledgment James McPhee and two reviewers for their comments, which have improved this manuscript. This research was supported by the Department of Civil Engineering at Facultad de Ciencias Fisicas y Matematicas, Universidad de Chile, under the CODELCO Grant 4501065855.

References

Barrett, B. S., R. D. Garreaud, and M. Falvey, 2009: Effect of the Andes Cordillera on Precipitation from a Midlatitude Cold Front. Mon. Wea. Rev., 137, 3092–3109.

Barros, A. P., G. Kim, E. Williams, and S. W.Nesbitt, 2004: Probing orographic controls in the Himalayas during the monsoon using satellite imagery. Nat. Hazards Earth Syst. Sci., 4, 29-51, doi:10.5194/nhess-4-29-2004, 2004.

Draxler, R. R., and G. D. Rolph, 2012: HYSPLIT (HYbrid Single-Particle Lagrangian Integrated Trajectory) Model access via NOAA ARL READY Website (http://ready.arl.noaa.gov/HYSPLIT.php). NOAA Air Resources Laboratory, Silver Spring, MD.

Durre I., R. S. Vose, and D. B. Wuertz, 2006: Overview of the Integrated Global Radiosonde Archive. J. Climate, 19, 53-68.

Falvey, M., and R. D. Garreaud, 2005: Moisture variability over the South American Altiplano during the South American Low Level Jet Experiment (SALLJEX) observing season. J. Geophys. Res., 110, D22105, doi:10.1029/2005JD006152.

Falvey, M., and R. Garreaud, 2007: Wintertime precipitation episodes in Central Chile: associated meteorological conditions and orographic influences. J. Hydrometeor., 8, 171-193.

Garreaud, R., and J. Rutllant, 1997: Summertime precipitation on the Andes of central Chile: climatological aspects (In Spanish). Atmosfera, 10, 191-211.

Garreaud, R., and J. M. Wallace, 1998: Summertime incursions of midlatitude air into the subtropical and tropical South America. Mon. Wea. Rev., 126, 2713-2733.

Garreaud, R., 1999: Multiscale analysis of the summertime precipitation over the central Andes. Mon. Wea. Rev., 127, 901-921.

Garreaud, R., 2009: The Andes climate and weather. Adv. Geosci., 7, 1-9.

Garreaud, R., 2013: Warm winter storms in Central Chile. J. Hydrometeor. doi:10.1175/JHM-D-12-0135.1, in press.

Giovannettone, J. P., and A. P. Barros, 2008: A Remote Sensing Survey of the Role of Landform on the Organization of Orographic Precipitation in Central and Southern Mexico. J. Hydrometeor, 9, 1267–1283.

Giovannettone, J. P., and A. P. Barros, 2009: Probing Regional Orographic Controls of Precipitation and Cloudiness in the Central Andes Using Satellite Data. J. Hydrometeor, 10, 167–182.

Golder Associates, 2009: Vulnerability to the risk of landslides in Los Sapos creek, El Teniente mine, Chile (In Spanish). Technical note. 31 pp.

Hall, D., and V. Salomonson. 2006: MODIS/Aqua Daily L3 Global 500m Grid, Version 5. December to February 2002-2008. Boulder, Colorado USA: National Snow and Ice Data Center.

Hall, D. K., G. A. Riggs, and V. V. Salomonson. 2006: MODIS/Terra Daily L3 Global 500m Grid, Version 5. December to February 2002-2008. Boulder, Colorado USA: National Snow and Ice Data Center.

Hall, D. K., and G. A. Riggs, 2007: Accuracy assessment of the MODIS snow products. Hydrol. Process. 21, 1534-1547.

Medina, S., R. A. Houze Jr., A. Kumar, and D. Niyogi, 2010: Summer monsoon convection in the Himalayan region: Terrain and land cover effects. Quart. J. Roy. Meteor. Soc., 136, 593-616.

Miller, A., 1976: The climate of Chile. World Survey of Climatology, W. Schwerdtfeger, Ed., Vol. 12, Elsevier, 113–130.

Prohaska, F., 1976: The climate of Argentina, Paraguay and Uruguay. World Survey of Climatology, W. Schwerdtfeger, Ed., Vol. 12, Elsevier, 13–73.

Rahn, D., and R. Garreaud, 2010: Marine boundary layer over the subtropical southeast Pacific during VOCALS-Rex. Part 1: Mean structure and diurnal cycle. Atmos. Chem. Phys., 10, 4491-4506, doi:10.5194/acp-10-4491-2010.

Rasmussen, K., and R. A. Houze, Jr., 2011: Orogenic convection in subtropical South America as seen by the TRMM satellite. Mon. Wea. Rev., 139, 2399-2420.

Romatschke, U., and R. A. Houze, Jr., 2010: Extreme summer convection in South America. J. Climate, 23, 3761-3791.

Romatschke, U., and R. A. Houze, Jr., 2013: Characteristics of precipitating convective systems accounting for the summer rainfall of tropical and subtropical South America. J. Hydrometeorol., 14, 25-46.

Saha, S., and Coauthors, 2010: The NCEP Climate Forecast System Reanalysis. Bull. Amer. Meteor. Soc., 91, 1015-1057.

Seluchi, M. E., F. A. Norte, P. Satyamurty, and S. C. Chou, 2003: Analysis of three situations of the Foehn effect over the Andes (Zonda wind) using the Eta-CPTEC regional model. Wea. Forecasting, 18, 481-501.

Sepulveda, S. A., and Padilla C., 2008: Rain-induced debris and mudflow triggerings factors assessment in the Santiago cordilleran foothills, central Chile. Nat. Hazards, 47, 201-215.

Vera, C., and Coauthors, 2006: The South American Low-Level Jet Experiment. Bull. Amer. Meteor. Soc., 87, 63-77.

Viale, M., and M. N. Nuñez, 2011: Climatology of winter orographic precipitation over the Subtropical Central Andes and associated synoptic and regional characteristics. J. Hydrometeor., 12, 481-507.

Viale, M., R. Houze, Jr., and K. Rasmussen, 2013: Upstream orographic enhancement of a narrow cold-frontal rainband approaching the Andes. Mon. Wea. Rev., 141, 1708–1730.

Whiteman, C. D., 2000: Mountain Meteorology: Fundamentals and Applications. Oxford University Press, 355 pp.

Wilks, D. S., 1995: Statistical Methods in the Atmospheric Sciences: An Introduction. Academic Press, 467 pp.

Tables

Table 1: Data source for all the stations and Coordinate and height for only the mountain stations (i.e., altitude > 1300m and a distance less than 50 km from the crest of the Andes, plotted by black circles with a white point in its center, see Fig. 2a) used in the study for summertime (Dec-Feb) 2005-2010 period. The horizontal gray line separates different cross-barrier regions defined in the text: low Chilean side, high mountain region and low Argentinean side, respectively (from up to down).

Data Source or Station name	ID	Lat (S)	Lon (W)	Height (m)	Number of station or Data Source	Gap (%)
Dirección General de Aguas – Chile	DGA				109	
Dirección Meteorológica de Chile	DMC				5	
Riecillos	**RIE**	32.93	70.35	1300	DGA	0
Lagunitas	**LAG**	33.08	70.25	2765	CEMA	0
El Yeso	**LGN**	33.67	70.08	2475	DGA	0
Sewell	**SEW**	34.08	70.38	2154	CODELCO	0
Punta de Vacas	**PVA**	32.85	69.75	2450	SSRH	0
Polvaredas	**POL**	32.74	69.66	2250	SSRH	0
Los Mayines	**MAY**	35.65	70.20	1660	SSRH	0
Subsecretaria de Recursos Hídricos - Argentina	SSRH				25	
Dirección de Agricultura y Contingencias Climáticas – Arg.	DACC				7	

Table 2: Coordinate,height, distance to the foot of the Andes, and missing data for radiosonde stations used in this study for summertime (Dec-Feb) 1998-2010 period. The data used correspond to observations at 1200 UTC.

Radiosonde Station name	ID	Lat (S)	Lon (W)	Height (m)	Aprox.distance to the foot of the Andes (km)	Gap (%)
Santo Domingo – Chile	SD	33.65	71.62	75	150	26
Mendoza – Argentina	MZ	32.83	68.78	704	30	55
Cordoba – Argentina	CB	31.32	64.22	474	500	20
Santa Rosa - Argentina	SR	36.56	64.27	191	500	14

Table 3: Basic statistics of rainy days classified as the TSW and TWW cases, and neither of both (NoR) observed at stations over the 1998-2010 period and located on (from left to right): the western slopes (Italic letter), the slopes inmidiately east of crest (underlined text), and farther east of the crest (normal text) but before the plains. The stations located on the western and inmediately east of the crest slopes are consider as mountain stations (see details in the text of section 2).

Variable\ID	Event	*Rei*	*Lag*	*Yes*	May	Vac	Pol	Usp	San	Gui	Pot
Latitude		*32.9*	*33.1*	*33.7*	35.6	32.9	32.7	32.6	32.5	33.0	33.0
Missing (%)		*4.2*	*0*	*0*	0	2.9	2.6	0	0	2.6	2.6
DJF mean (mm)	TSW	*1.7*	*6.4*	*9.2*	7.8	0	0.2	0.9	1.5	0.9	2.2
	TWW	*5.2*	*27.2*	*7.4*	4.7	4.1	5.7	15.1	15.1	11.6	6.8
	NoR	*3.4*	*0.5*	*0.1*	9.9	5.4	10.4	62.1	99.8	60.9	69.3
Daily mean (mm)	TSW	*3.8*	*5.2*	*10*	11.2	0.5	1.0	4.1	6.5	12	14.3
	TWW	*4.5*	*4.2*	*3.7*	6.8	3.8	5.0	8.2	8.2	4.4	5.2
	NoR	*8.7*	*0.3*	*0.5*	5.8	6.4	4.0	7.1	10.2	4.2	5.7
Frequency (days)	TSW	*6*	*16*	*12*	9	1	2	3	3	1	2
	TWW	*15*	*85*	*26*	9	14	15	24	24	34	17
	NoR	*5*	*21*	*3*	22	11	34	114	127	189	159
Accumulated (%)	TSW	*17*	*19*	*55*	35	0	1	1	1	1	3
	TWW	*50*	*80*	*44*	21	43	35	19	13	16	9
	NoR	*33*	*1*	*1*	44	57	64	79	86	83	89

Figures Captions

Table 1: Data source for all the stations and Coordinate and height for only the mountain stations (i.e., altitude > 1300m and a distance less than 50 km from the crest of the Andes, plotted by black circles with a white point in its center, see Fig. 2a) used in the study for summertime (Dec-Feb) 2005-2010 period. The horizontal gray line separates different cross-barrier regions defined in the text: low Chilean side, high mountain region and low Argentinean side, respectively (from up to down).

Table 2: Coordinate,height, distance to the foot of the Andes, and missing data for radiosonde stations used in this study for summertime (Dec-Feb) 1998-2010 period. The data used correspond to observations at 1200 UTC.

Table 3: Basic statistics of rainy days classified as the TSW and TWW cases, and neither of both (NoR) observed at stations over the 1998-2010 period and located on (from left to right): the western slopes (Italic letter), the slopes inmidiately east of crest (underlined text), and farther east of the crest (normal letter) but before the plains. The stations located on the western and inmediately east of the crest slopes are consider as mountain stations (see details in the text of section 2).

Figure 1: Summer (DJF) mean 850 hPa map of geopotential height (contoured every 20m), temperature (shaded), and wind vectors (m s^{-1}) obtained from CFSR reanalysis data over the period 1998-2010. The box corresponds to the area of the plot in Figure 2a. The radiosonde locations are indicated by circles and its respective ID (see Table 2).

(b) Mean 32º-36ºS cross-barrier plot of cloud frequency (reflectivity data between -27 and 25 dBZ) derived from CloudSat Level 3 data for DJF month over 2007-2010 period.

Figure 2: (a) Summertime (DJF) mean precipitation (mm), (b) frequency of rainy days (%), and (c) percentage of the annual total (mm) for the 2005-2010 period. The mountain stations are plotted by black circles with a white cross in its center in panel (a), while in panel (b) and (c) the mountain, low Chilean and low Argentinean stations are plotted with square, gray and black filled circles, respectively. The mountain stations are defined by an altitude higher than 1300 m and by a distance lesser than 50 km of the Argentine-Chile frontier (i.e., the line water divide which approximately represent the crest of the Andes).

Figure 3: Summertime (DJF) cloud frequency derived from MODIS data on board of (a) the satellite TERRA at moon hours (~12 LST) and (b) the satellite AQUA at afternoon hours (~16 LST), for the 2002-2010 period. Panel (c) shows the mean cross-barrier section (meridionally averaged between 32.5º and 34.5º S) of the topography (black line), and of the cloud frequency in the moon (red line) and afternoon (blue line). Panel (d) shows a particular cross-barrier section at 33.4ºS (indicated by the white line in b) of the topography and cloud frequency in the afternoon. The blue circles in panels (a) and (b) correspond to the locations of mountain stations. The dashed white line corresponds to the Argentina-Chile frontier and the thin black and gray lines to the topography height of 1000 m, 3000 m and 5500 m in panels (a) and (b).

Figure 4: Summertime (DJF) mean fields of 10m-wind (vectors are plotted in m s^{-1} every 2 point for better readability) and of divergence (shaded $10^{-5}s^{-1}$) at (a) 1800 UTC (1500 LST) and (b) 0600 UTC (0300 LST). The altitude lines of 0 m, 1000 m, and 3000 m are ploted in black colors. The mean fields were plotted using the Reanalysis CFSR surface data with 0.3125° of resolution over the 1998-2010 period. (c) Summertime wind intensity (solid line in m s^{-1}) and wind direction (dotted line) hourly mean for LAG observations located on the western slope (also See Table 1).

Figure 5: Mean (left) and normalized anomalies (right) of 500-hPa temperature and geopotential height for the TSW (top panels) and TWW (bottom panels) cases. (a)-(c) Temperature is shaded every 3°C and geopotential height is contoured every 50 m. (b)-(d) Normalized anomalies of temperature is shaded every 0.3σ and of geopotential height is contoured every 0.3σ.

Figure 6: Scatter plots of u-wind and v-wind (m s^{-1}) at 500-hPa level obtained from 12UTC rawinsonde observations at (a) Santo Domingo, (b) Mendoza, (c) Santa Rosa, and (d) Cordoba stations over the 1998-2010 period. The gray, red, and blue circles correspond to all summer days, and the TWW and TSW rainy days, respectively. The bigger circles with a white cross inside correspond to the mean u-, and v- wind of each group.

Figure 7: Left panels show normalized anomalies of temperature (shaded every 0.3σ) and of geopotential height (contoured every 0.3σ) at 850-hPa level for the (a) TSW and (c) TWW Cases. Right panels show normalized anomalies (shaded every 0.3σ) and mean

fields (contoured) of specific humidity at 700- hPa level, and the mean wind vectors at 850 hPa level for the (b) TSW and (d) TWW Cases. The altitude lines of 1500 m (left panels), and 3000 m (rigth panels) are also plotted in black color.

Figure 8: SkewT-log p diagram for the mean composite of Temperature and dew point temperature for the TSW (black dot-dash lines), the TWW (black solid lines) cases, and for the mean DJF (gray solid lines) at (a) Santo Domingo and (b) Mendoza rawinsonde stations. Along with skewT-log p diagram are plotted the mean composite wind profiles (half barb = 5 km h^{-1}, full barb = 10 km h^{-1} and one pennant = 50 km h^{-1}).

Figure 9: (a) Composite profiles of the observed lapse rates at Santo Domingo (SD) radiosonde stations for the TSW (black lines) and TWW (dark gray line) rainy days, and the NonRainy days (light gray line). The lapse rates were calculated using the differences in temperatures and geopotential heights between successive standard vertical pressure levels. (b) Vertical profiles of the difference between the temperatures observed at the same vertical level during the rainy day and two days before for the TSW (black), and the TWW (dark gray) rainy days, and the non-rainy days (light gray) at SD (solid lines) and MZ (dashed lines) radiosonde stations.

Figure 10: Summer (DJF) cloud frequency for the TSW rainy days [upper panels, (a)-(d)], the TWW rainy days [middle panels, (b)-(e)], and the Non rainy days [lower panels, (c)-(f)] obtained from MODIS data on board of TERRA (left panels) and AQUA (right panels) satellites, which pass over western South America at noon and afternoon hours, respectively. In each panel, the white line corresponds to the Argentina-Chile border

(representative of the crest line), the black lines correspond to the topography height of 1000 m and 3000 m, and the blue circles represent the mountain weather station locations.

Figure 11: Visible imagery from the GOES-13 satellite at (a) 1800 UTC 25 February 2008 and (b) 2100 UTC 11 December 2010, representative of TSW and TWW cases, respectively. The Chile-Argentina border (representative of the Andean crest line) is plotted using red line and the yellow circles represent weather station locations used in this study (see also Table 1).

Figure 12: Vertical profiles of mean (solid lines) and normalized anomalies (dot-shaded lines) of specific humidity for TSW (black lines) and TWW (gray lines) cases at (a) Santo Domingo and (b) Mendoza radiosonde stations.

Figure 13: Specific humidity (g Kg^{-1}) observed at (a) morning, (b) afternoon, and (c) evening at LAG (squared symbols) and PVA (asterisk sympols) mountain stations, and in the layer 850-700hPA at Santo Domingo (SD) sounding station on the Pacific coast (circle sympols) for the TWW (gray colour) and TSW (black colour) rainy days, and for the No-Rainy days (NoR in light gray). The observational time are 8, 17, and 20 Local Time for LAG station; 9 and 21 for SD sounding; and 9, 15, and 21 for PVA station.

Figure 14: Map of 48h backward trajectories ending at points on the western and eastern slope of the Andes (yellow circles) at 4 km above sea level for (a) TSW and (f) TWW cases during the 2005-2010 subperiod. Time series of parcel's mean height,

temperature, specific humidity, and potential temperature equivalent for trajectories shown in top panels associated with the TSW (left panels, (b)-(e)) and TWW (right panels, (g)-(j)) cases. The red and blue lines indicate time series of trajectories ending at point on the western and eastern slope of the Andes, respectively.

Figure 15: Vertical profile of daily mean zonal moisture flux (m s^{-1} g kg^{-1}) at (a) the western and (b) the eastern side of the Andes for the TWW (blue) and TSW (red) rainy days, and the non-raining days (black). The zonal moisture flux was calculated using the CSFR data, and meridionally averaged between 32°S and 35°S along the 71°W and 68.5°W meridian on the western and eastern foothills of the Andes, respectively.

Figure 16: Cross-barrier schematic representation of the weather conditions during (a) non rainy days, (b) TWW rainy days, and (c) TSW rainy days.

Figures

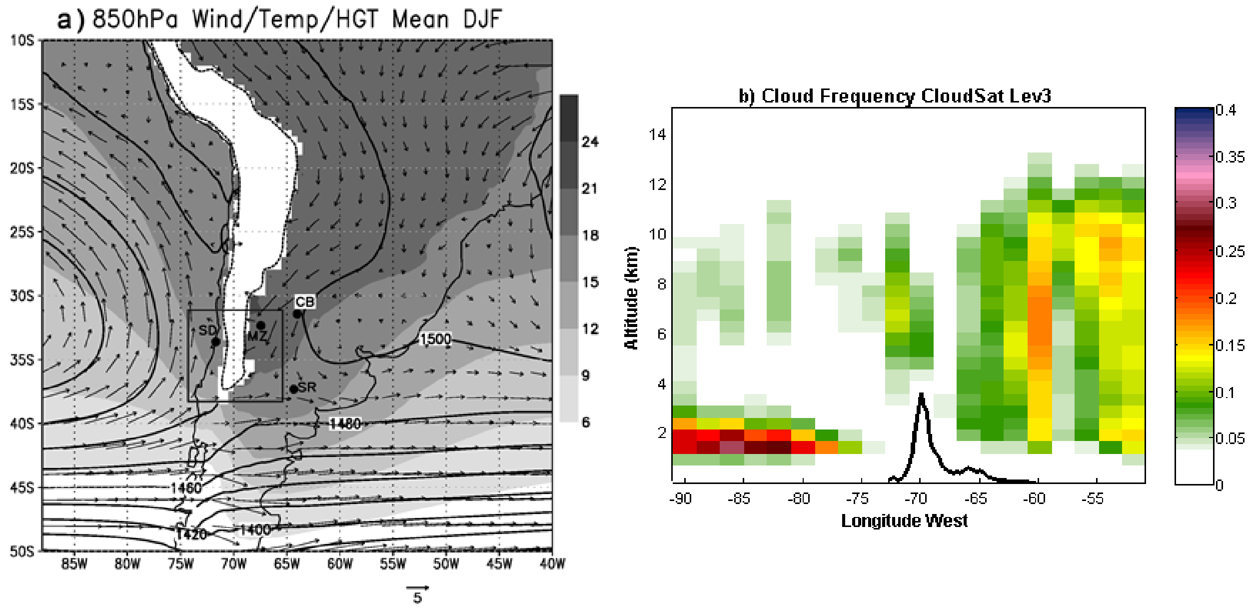

Figure 1: Summer (DJF) mean 850 hPa map of geopotential height (contoured every 20m), temperature (shaded), and wind vectors (m s^{-1}) obtained from CFSR reanalysis data over the period 1998-2010. The box corresponds to the area of the plot in Figure 2a. The radiosonde locations are indicated by circles and its respective ID (see Table 2). (b) Mean 32º-36ºS cross-barrier plot of cloud frequency (reflectivity data between -27 and 25 dBZ) derived from CloudSat Level 3 data for DJF month over 2007-2010 period.

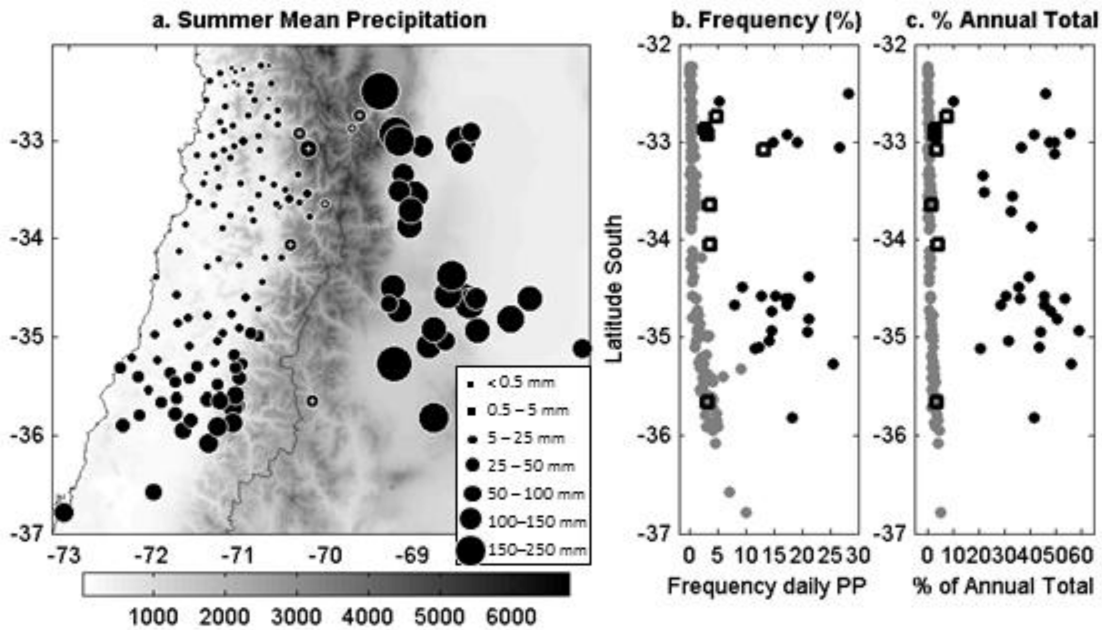

Figure 2: (a) Summertime (DJF) mean precipitation (mm), (b) frequency of rainy days (%), and (c) percentage of the annual total (mm) for the 2005-2010 period. The mountain stations are plotted by black circles with a white cross in its center in panel (a), while in panel (b) and (c) the mountain, low Chilean and low Argentinean stations are plotted with square, gray and black filled circles, respectively. The mountain stations are defined by an altitude higher than 1300 m and by a distance lesser than 50 km of the Argentine-Chile frontier (i.e., the line water divide which approximately represent the crest of the Andes).

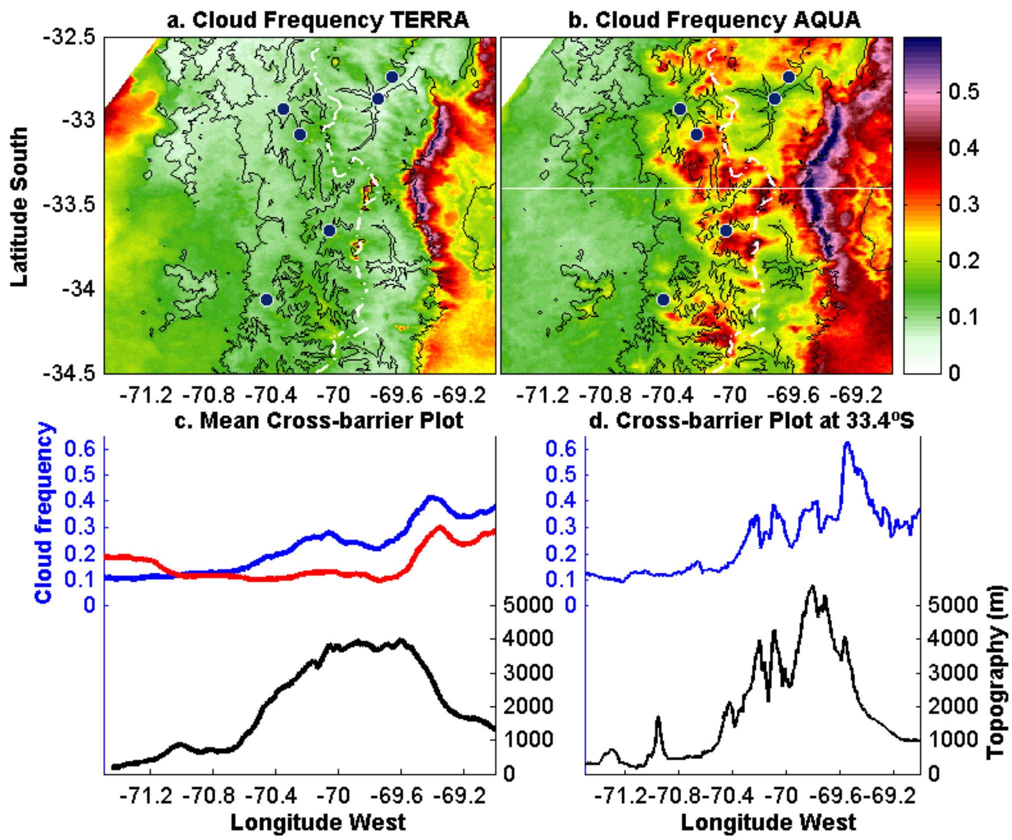

Figure 3: Summertime (DJF) cloud frequency derived from MODIS data on board of (a) the satellite TERRA at moon hours (~12 LST) and (b) the satellite AQUA at afternoon hours (~16 LST), for the 2002-2010 period. Panel (c) shows the mean cross-barrier section (meridionally averaged between 32.5º and 34.5º S) of the topography (black line), and of the cloud frequency in the moon (red line) and afternoon (blue line). Panel (d) shows a particular cross-barrier section at 33.4ºS (indicated by the white line in b) of the topography and cloud frequency in the afternoon. The blue circles in panels (a) and (b) correspond to the locations of mountain stations. The dashed white line corresponds to the Argentina-Chile frontier and the thin black and gray lines to the topography height of 1000 m, 3000 m and 5500 m in panels (a) and (b).

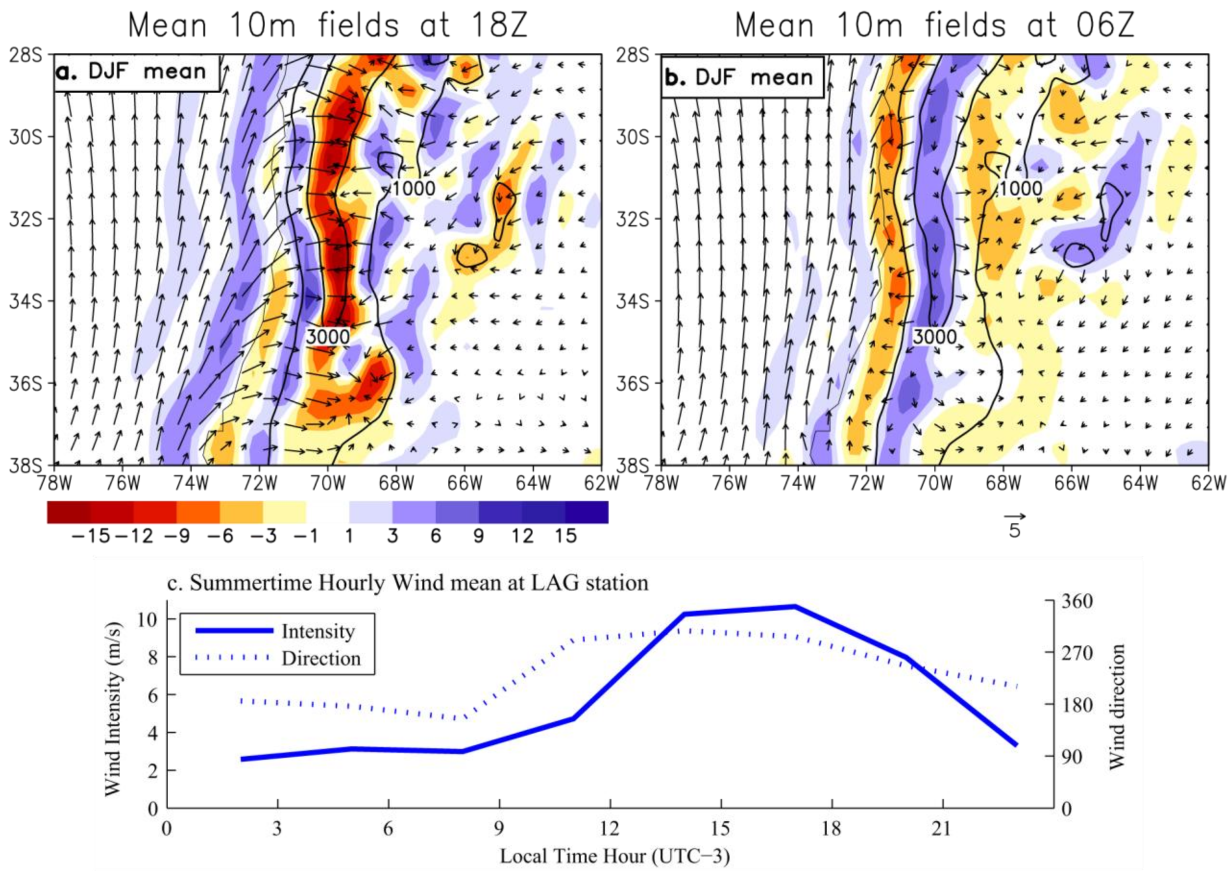

Figure 4: Summertime (DJF) mean fields of 10m-wind (vectors are plotted in $m\ s^{-1}$ every 2 point for better readability) and of divergence (shaded $10^{-5} s^{-1}$) at (a) 1800 UTC (1500 LST) and (b) 0600 UTC (0300 LST). The altitude lines of 0 m, 1000 m, and 3000 m are plotted in black colors. The mean fields were plotted using the Reanalysis CFSR surface data with 0.3125° of resolution over the 1998-2010 period. (c) Summertime wind intensity (solid line in $m\ s^{-1}$) and wind direction (dotted line) hourly mean for LAG observations located on the western slope (also See Table 1).

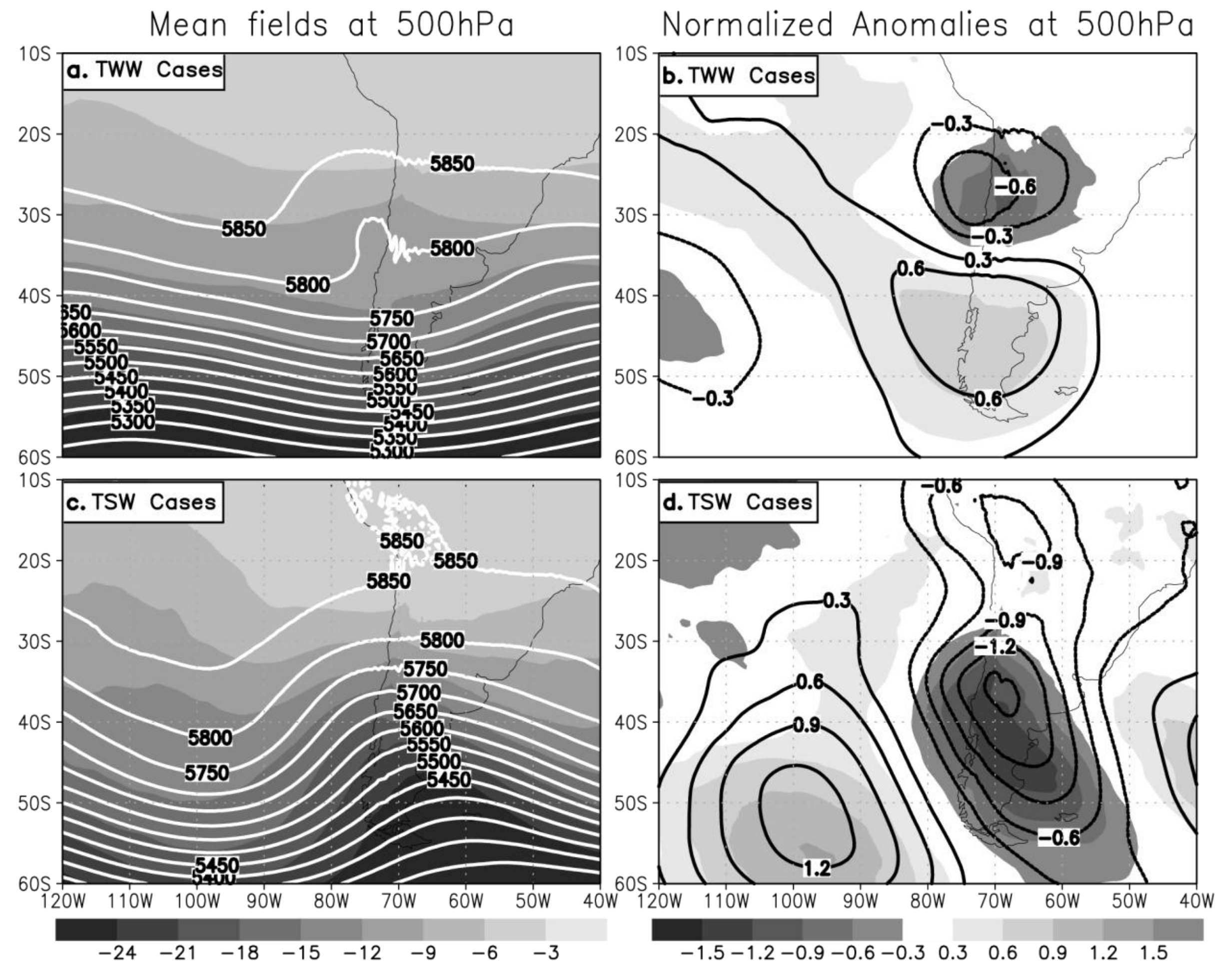

Figure 5: Mean (left) and normalized anomalies (right) of 500-hPa temperature and geopotential height for the TSW (top panels) and TWW (bottom panels) cases. (a)-(c) Temperature is shaded every 3°C and geopotential height is contoured every 50 m. (b)-(d) Normalized anomalies of temperature is shaded every 0.3σ and of geopotential height is contoured every 0.3σ.

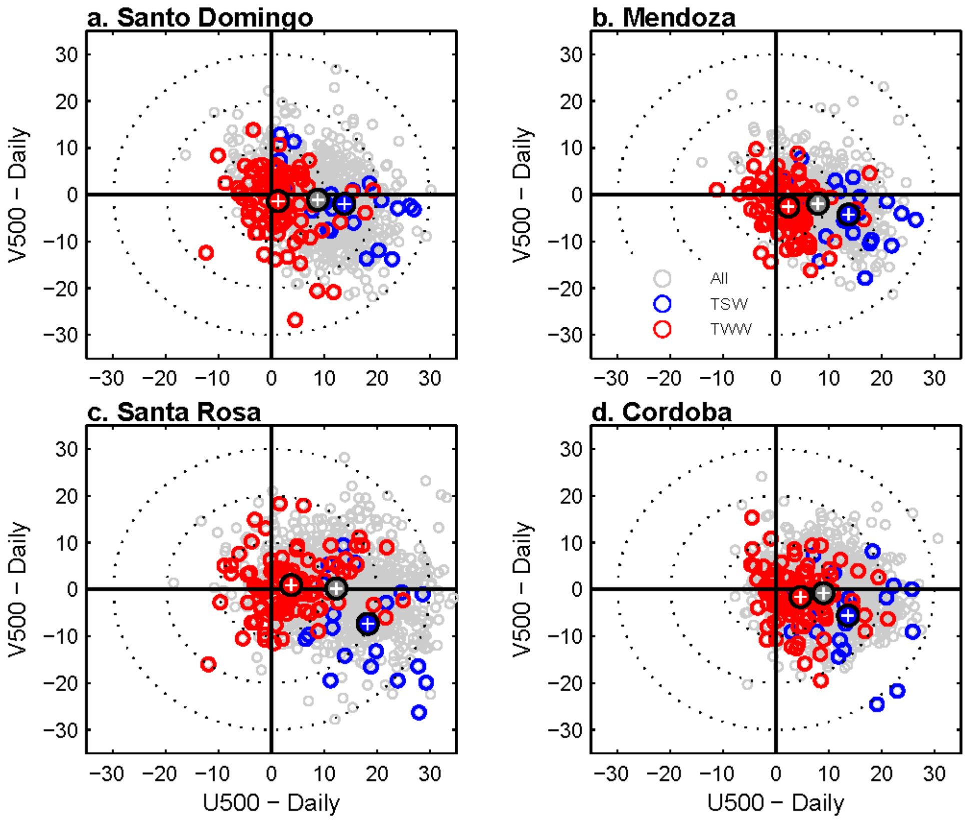

Figure 6: Scatter plots of u-wind and v-wind at 500-hPa level obtained from 12UTC rawinsonde observations at (a) Santo Domingo, (b) Mendoza, (c) Santa Rosa, and (d) Cordoba stations over the 1998-2010 period. The gray, red, and blue circles correspond to all summer days, and the TWW and TSW rainy days, respectively. The bigger circles with a white cross inside correspond to the mean u-, and v- wind of each group.

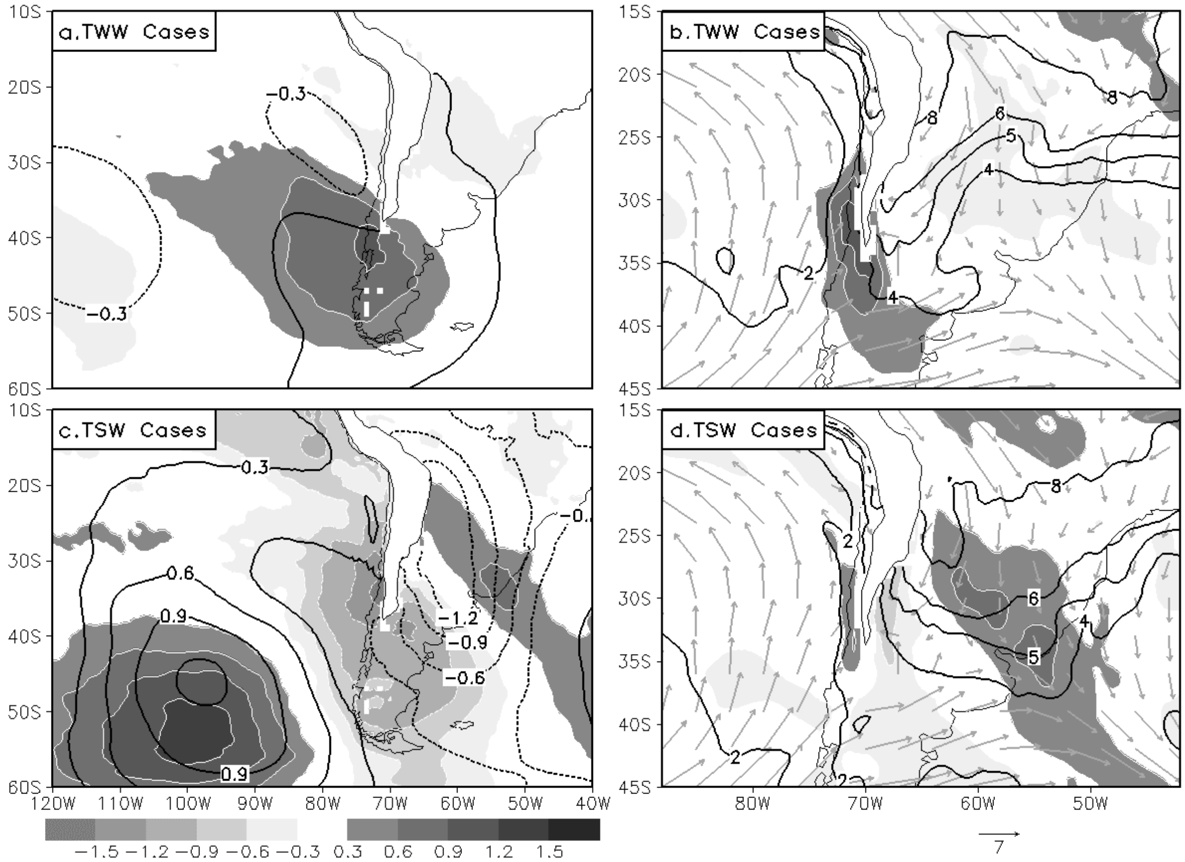

Figure 7: Left panels show normalized anomalies of temperature (shaded every 0.3σ) and of geopotential height (contoured every 0.3σ) at 850-hPa level for the (a) TSW and (c) TWW Cases. Right panels show normalized anomalies (shaded every 0.3σ) and mean fields (contoured) of specific humidity at 700- hPa level, and the mean wind vectors at 850 hPa level for the (b) TSW and (d) TWW Cases. The altitude lines of 1500 m (left panels), and 3000 m (rigth panels) are also plotted in black color.

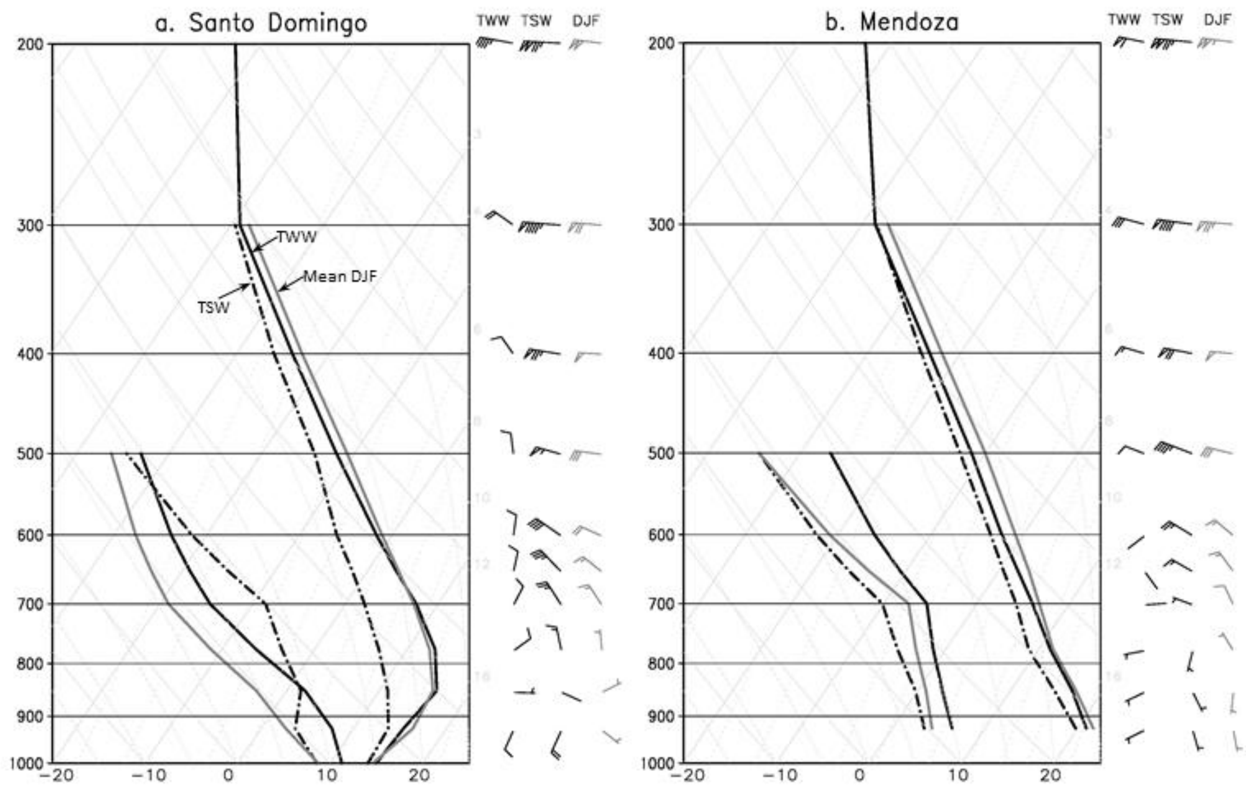

Figure 8: SkewT-log p diagram for the mean composite of Temperature and dew point temperature for the TSW (black dot-dash lines), the TWW (black solid lines) cases, and for the mean DJF (gray solid lines) at (a) Santo Domingo and (b) Mendoza rawinsonde stations. Along with skewT-log p diagram are plotted the mean composite wind profiles (half barb = 5 km h^{-1}, full barb = 10 km h^{-1} and one pennant = 50 km h^{-1}).

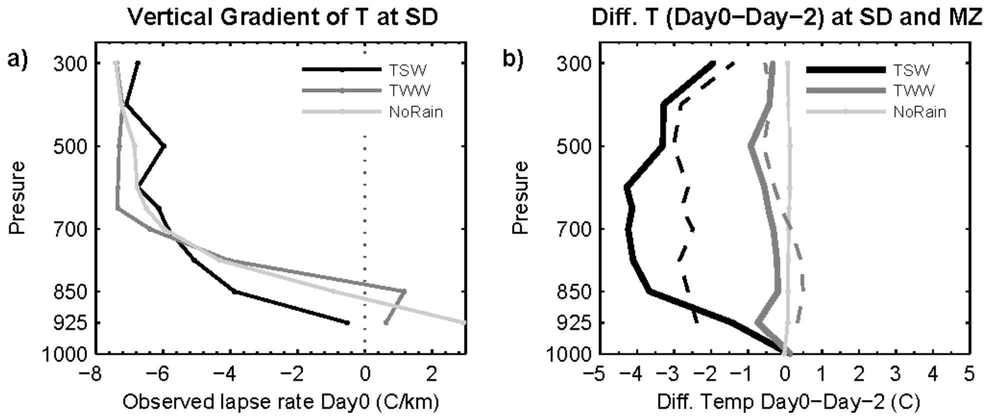

Figure 9: (a) Composite profiles of the observed lapse rates at Santo Domingo (SD) radiosonde stations for the TSW (black lines) and TWW (dark gray line) rainy days, and the NonRainy days (light gray line). The lapse rates were calculated using the differences in temperatures and geopotential heights between successive standard vertical pressure levels. (b) Vertical profiles of the difference between the temperatures observed at the same vertical level during the rainy day and two days before for the TSW (black), and the TWW (dark gray) rainy days, and the non-rainy days (light gray) at SD (solid lines) and MZ (dashed lines) radiosonde stations.

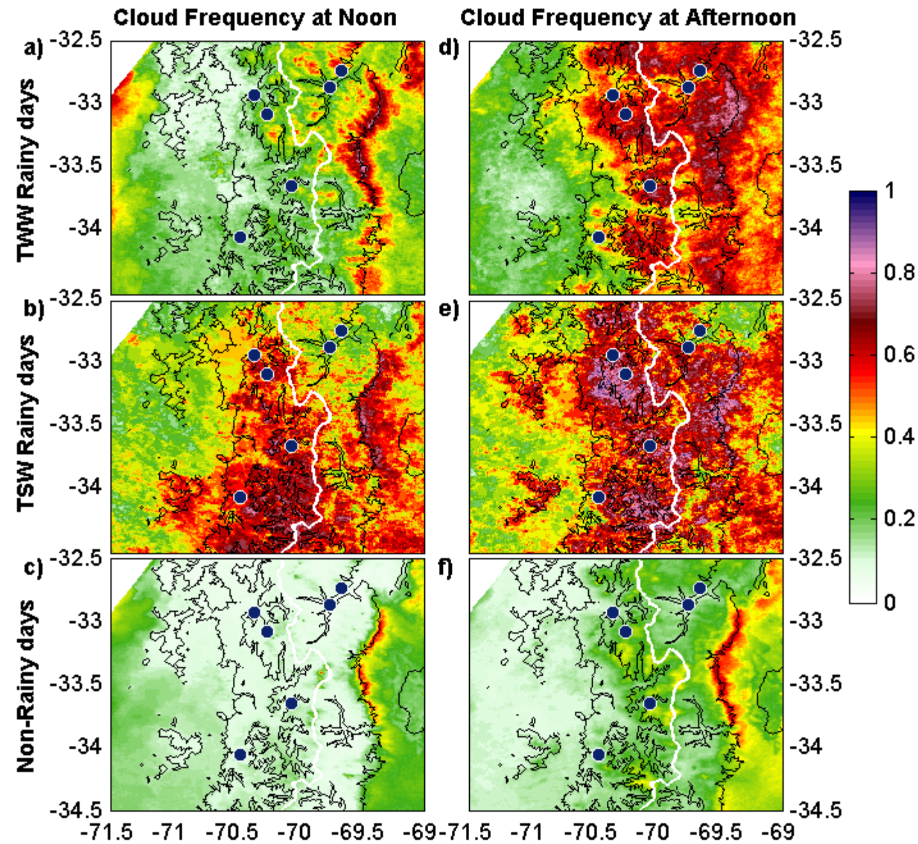

Figure 10: Summer (DJF) cloud frequency for the TSW rainy days [upper panels, (a)-(d)], the TWW rainy days [middle panels, (b)-(e)], and the Non rainy days [lower panels, (c)-(f)] obtained from MODIS data on board of TERRA (left panels) and AQUA (right panels) satellites, which pass over western South America at noon and afternoon hours, respectively. In each panel, the white line corresponds to the Argentina-Chile border (representative of the crest line), the black lines correspond to the topography height of 1000 m and 3000 m, and the blue circles represent the mountain weather station locations.

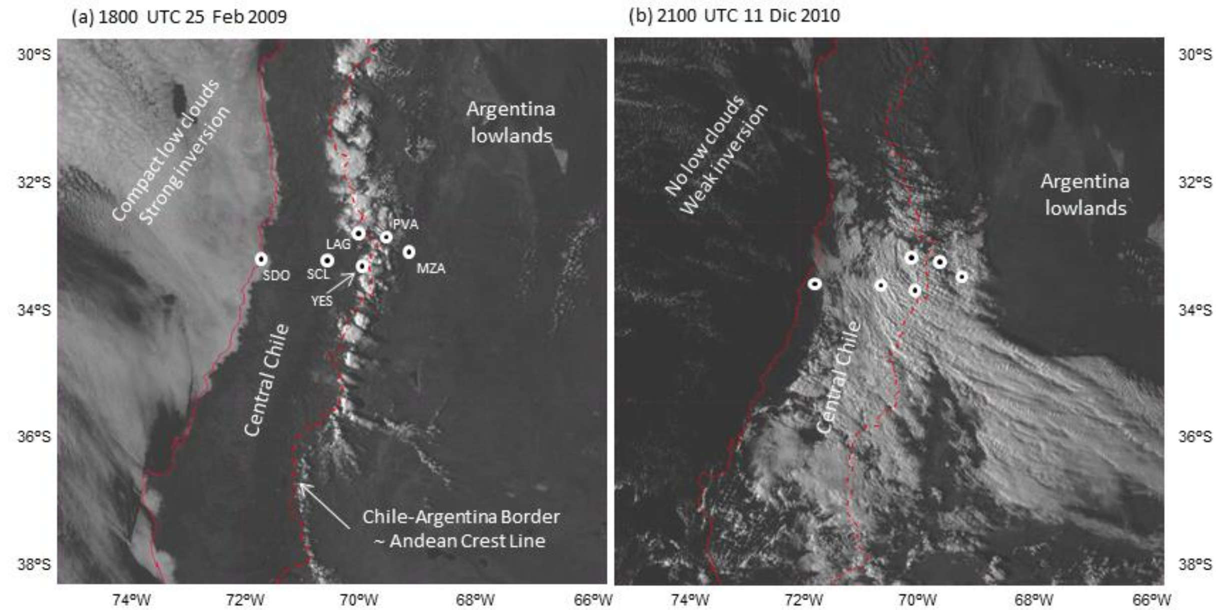

Figure 11: Visible imagery from the GOES-13 satellite at (a) 1800 UTC 25 February 2008 and (b) 2100 UTC 11 December 2010, representative of TSW and TWW cases, respectively. The Chile-Argentina border (representative of the Andean crest line) is plotted using red line and the white circles represent weather station locations used in this study (see also Table 1).

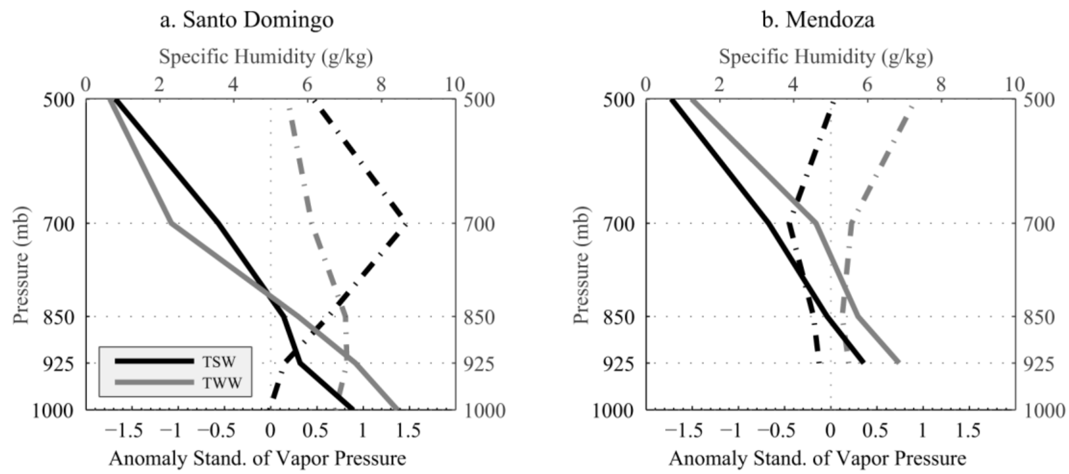

Figure 12: Vertical profiles of mean (solid lines) and normalized anomalies (dot-shaded lines) of specific humidity for TSW (black lines) and TWW (gray lines) cases at (a) Santo Domingo and (b) Mendoza radiosonde stations.

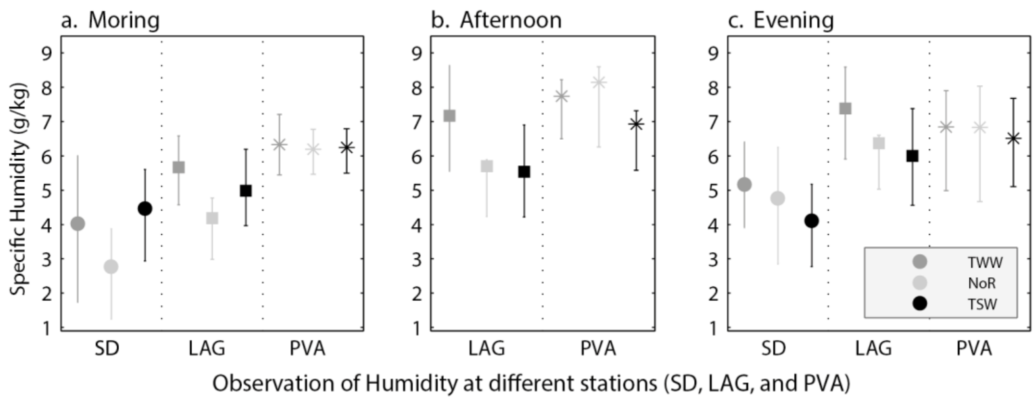

Figure 13: Specific humidity (g Kg^{-1}) observed at (a) morning, (b) afternoon, and (c) evening at LAG (squared symbols) and PVA (asterisk sympols) mountain stations, and in the layer 850-700hPA at Santo Domingo (SD) sounding station on the Pacific coast (circle sympols) for the TWW (gray colour) and TSW (black colour) rainy days, and for the No-Rainy days (NoR in light gray). The observational time are 8, 17, and 20 Local Time for LAG station; 9 and 21 for SD sounding; and 9, 15, and 21 for PVA station.

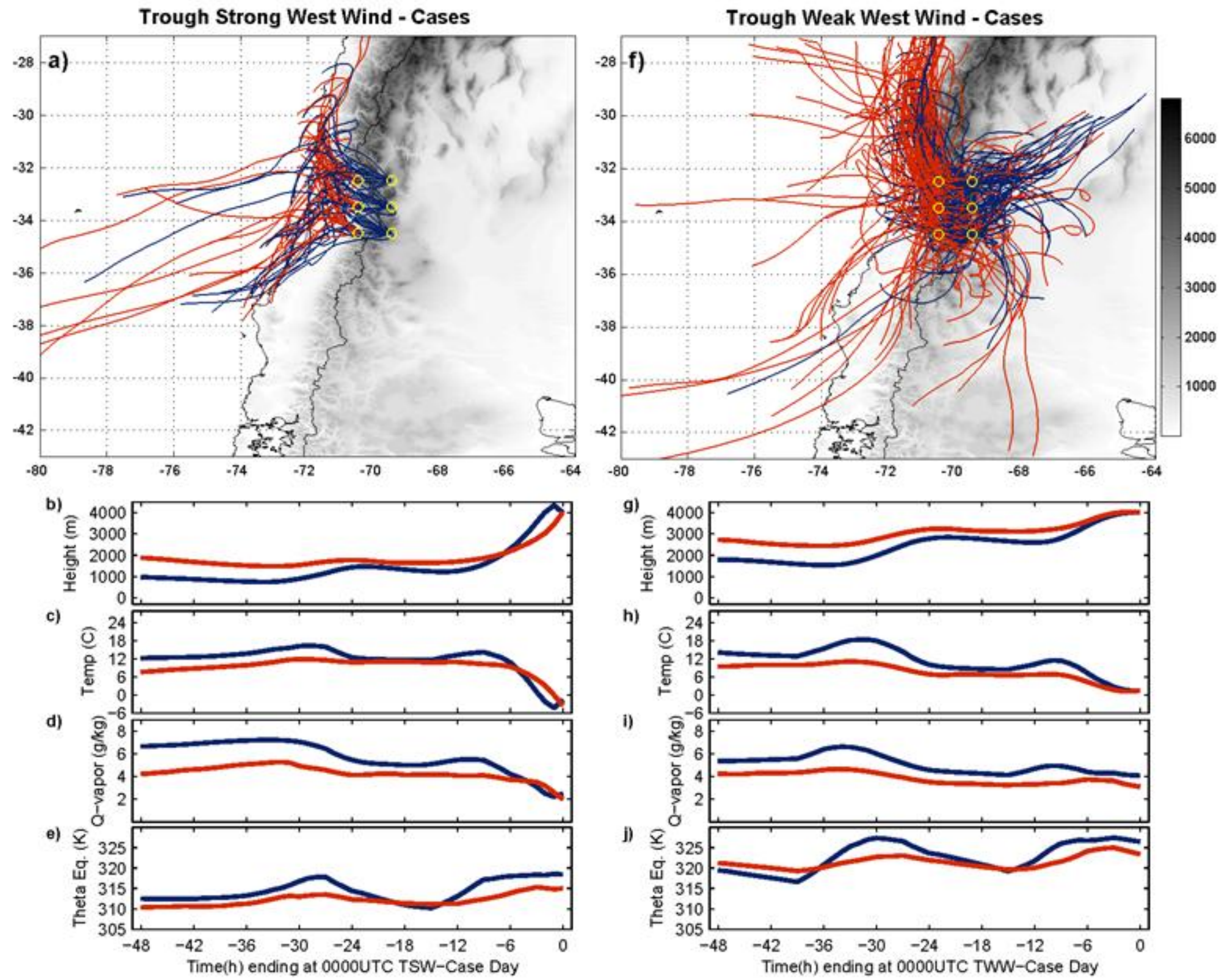

Figure 14: Map of 48h backward trajectories ending at points on the western and eastern slope of the Andes (yellow circles) at 4 km above sea level for (a) TSW and (f) TWW cases during the 2005-2010 subperiod. Time series of parcel's mean height, temperature, specific humidity, and potential temperature equivalent for trajectories shown in top panels associated with the TSW (left panels, (b)-(e)) and TWW (right panels, (g)-(j)) cases. The red and blue lines indicate time series of trajectories ending at point on the western and eastern slope of the Andes, respectively.

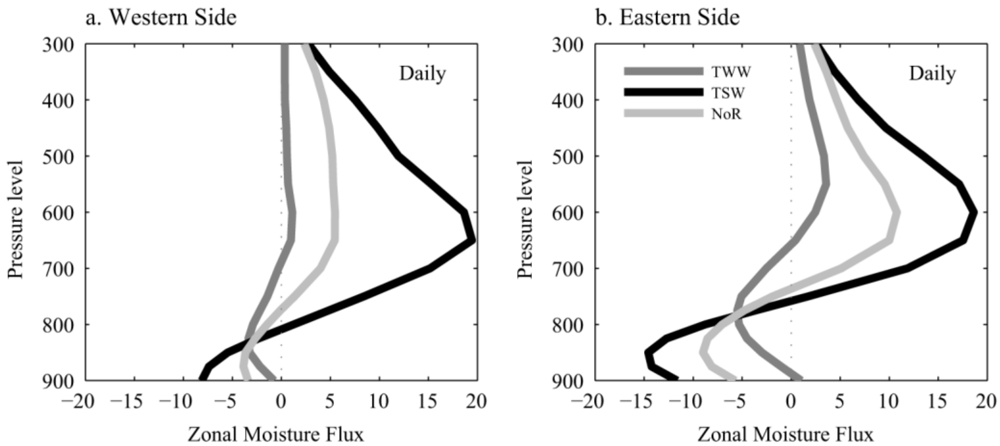

Figure 15: Vertical profile of zonal moisture flux (m s^{-1} g kg^{-1}) daily mean at (a) the western and (b) the eastern side of the Andes for the TWW (blue) and TSW (red) rainy days, and the non-raining days (black). The zonal moisture flux was calculated using the CSFR data, and meridionally averaged between 32°S and 35°S along the 71°W and 68.5°W meridian on the western and eastern foothills of the Andes, respectively.

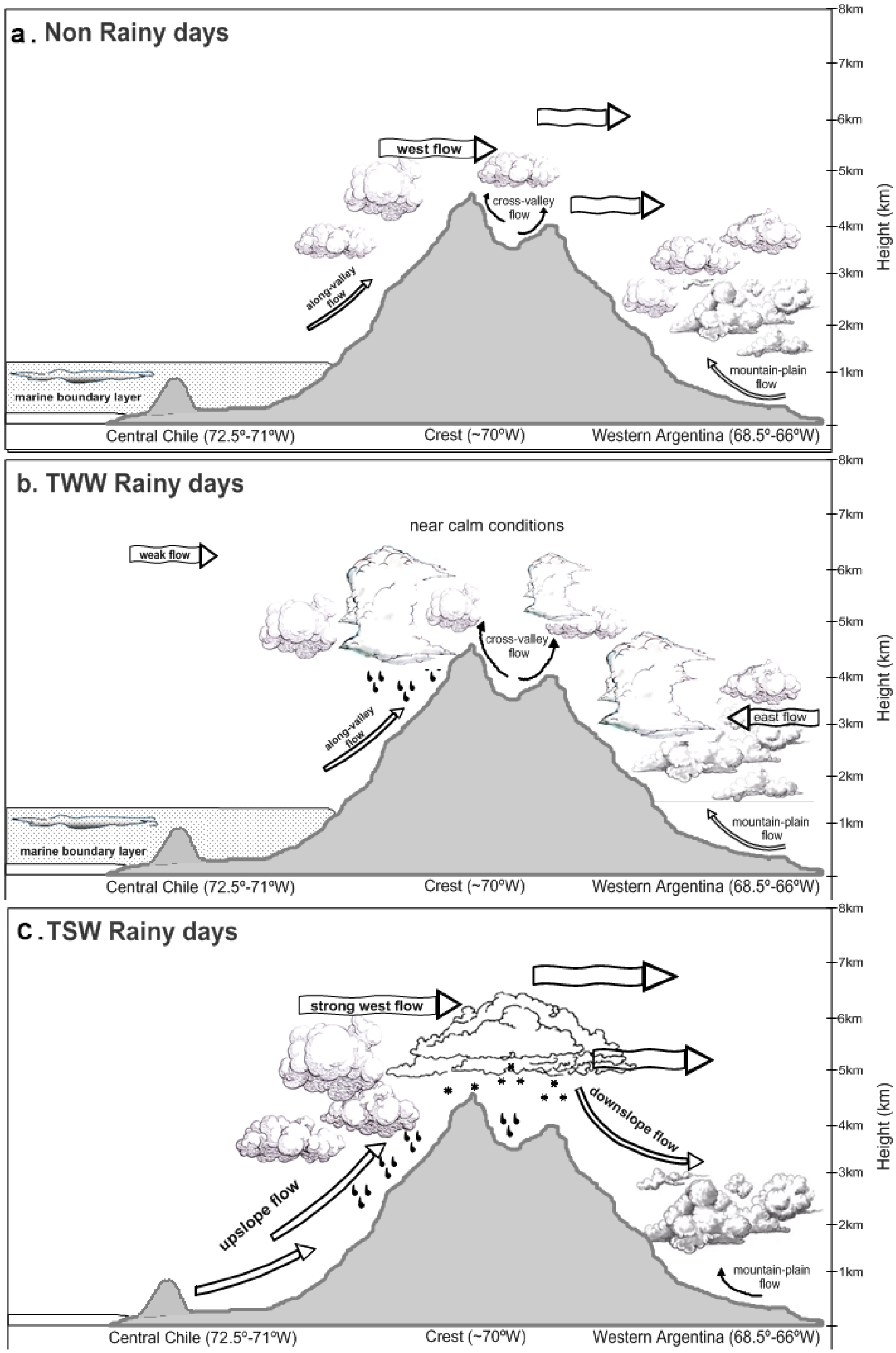

Figure 16: Cross-barrier schematic representation of the weather conditions during (a) non rainy days, (b) TWW rainy days, and (c) TSW rainy days.